Vertical and In-Plane Heterostructures from WS_2/MoS_2 Monolayers

Yongji Gong[1, 2 †], Junhao Lin[3, 4 †], Xingli Wang[5 †] Gang Shi[2], Sidong Lei[2], Zhong Lin[6], Xiaolong Zou[2], Gonglan Ye[2], Robert Vajtai[2], Boris I. Yakobson[2], Humberto Terrones[7], Mauricio Terrones[6, 8], Beng Kang Tay[5], Jun Lou[2], Sokrates T. Pantelides[3, 4], Zheng Liu[5], Wu Zhou[3 *], Pulickel M. Ajayan[1,2 *]

1 Department of Chemistry, Rice University, Houston, TX 77005, USA
2 Department of Materials Science & NanoEngineering, Rice University, Houston, TX 77005, USA
3 Materials Science & Technology Division, Oak Ridge National Lab, Oak Ridge, TN 37831, USA
4 Department of Physics and Astronomy, Vanderbilt University, Nashville, TN 37235, USA
5 School of Materials Science and Engineering, School of Electrical and Electronic Engineering Nanyang Technological University, 639798, Singapore
6 Department of Physics and Center for 2-Dimensional and Layered Materials, The Pennsylvania State University, University Park, Pennsylvania 16802, USA
7 Department of Physics, Applied Physics and Astronomy, Rensselaer Polytechnic Institute, Johnson-Rowland Science Center, 110 Eighth Street, Troy, NY 12180, USA.
8 Department of Chemistry, Department of Materials Science and Engineering & Materials Research Institute, The Pennsylvania State University, University Park, PA 16802, USA
† Y.G., J.L. and X.W. contributed equally to this work
* Corresponding authors: wu.zhou.stem@gmail.com; ajayan@rice.edu

Layer-by-layer stacking or lateral interfacing of atomic monolayers has opened up new unprecedented opportunities to engineer two-dimensional (2D) heteromaterials. Fabrication of such artificial heterostructures with atomically clean and sharp interfaces, however, is challenging. Here, we report a one-step growth strategy for the creation of high-quality vertically stacked as well as in-plane interconnected heterostructures of WS_2/MoS_2 via control of the growth temperature. Vertically stacked bilayers with WS_2 epitaxially grown on top of MoS_2 monolayer are formed with preferred stacking order at high temperature. Strong interlayer excitonic transition is observed due to the type II band alignment and to the clean interface of these bilayers. Vapor growth at low temperature, on the other hand, leads to lateral epitaxy of WS_2 on MoS_2 edges, creating seamless and atomically sharp in-plane heterostructures that generate strong localized photoluminescence enhancement and intrinsic p-n junctions. The fabrication of heterostructures from monolayers, using simple and scalable growth, paves the way for the creation of unprecedented two-dimensional materials with exciting properties.

Heterostructures have been the essential elements in modern semiconductor industry, and play a crucial role in high-speed electronics and opto-electronic devices[1,2]. Beyond conventional semiconductors, two-dimensional (2D) materials provide a wide range of basic building blocks with distinct optical and electrical properties, including graphene[3], hexagonal boron nitride[4,5], and transition-metal dichalcogenides (TMDs)[6-9]. These atomic monolayers could also be combined to create van der Waals heterostructures, where monolayers of multiple 2D materials are stacked vertically layer-by-layer, or stitched together seamlessly in plane to form lateral heterojunctions. Many novel physical properties have been explored on such van der Waals heterostructures, and devices with improved performance have been demonstrated[10-14]. The lateral heterojunctions could also lead to exciting new physics and applications. For example, the semiconducting monolayer TMDs can serve as building blocks for p-n junctions and other opto-electronic devices[15-17]. However, the fabrication of 2D heterostructures with clean and sharp interfaces, essential for preserving opto-electronic properties driven by the interlayer or intralayer coupling, remains challenging. Van der Waals heterostructures could be created by stacking different 2D materials using mechanical transfer techniques[12]. However, the stacking orientation cannot be precisely controlled, and the interface between layers can be easily contaminated[18,19], not to mention the challenge for massive production of the samples. Lateral heterostructures, in contrast, can only be created via growth. Both vertical and in-plane heterostructures of semimetallic graphene and insulating h-BN have been recently demonstrated via chemical vapor deposition (CVD)[20-24]; however, direct growth of heterostructures consisting of different semiconducting monolayers has not been achieved.

Here, we report a scalable single-step vapor phase growth process for the creation of highly crystalline vertical stacked bilayers and in-plane interconnected WS_2/MoS_2 heterostructures, respectively, under different growth temperature. Atomic resolution scanning transmission electron microscopy (STEM) imaging reveals that high temperature growth yields predominantly vertically stacked bilayers with WS_2 epitaxially grown on top of the MoS_2 monolayer, following the preferred 2H stacking. In contrast, the low temperature growth creates mostly lateral heterostructures of WS_2 and MoS_2 within single hexagonal monolayer lattice, with atomically sharp heterojunctions along both the zigzag and armchair directions.

The vertical and lateral heterostructures are further verified by Raman and photoluminescence (PL) spectroscopy characterization. Strong interlayer or intralayer excitonic interaction between MoS_2 and WS_2 are observed by PL spectroscopy for the first time on these two types of heterostructures, owing to their clean and sharp interfaces. Specifically, a new bandgap of 1.42 eV is observed in the bilayer heterostructure, arising from the interlayer excitonic transition between MoS_2 and WS_2[25,26]; whereas a strong localized PL enhancement is observed at the lateral interface between MoS_2 and WS_2, presumably due to the increased excitonic recombination of the as-generated electron-hole pairs at the atomically sharp interface[27]. These two types of heterostructures are further demonstrated to be building blocks for high mobility field effect transistors (FET) and planar monolayer p-n junctions, indicating their potential for constructing unique devices.

Synthesis and Morphology

Figure 1I shows the scheme for the growth of WS_2/MoS_2 heterostructures. Molybdenum trioxide (MoO_3) powder is placed in front of the bare SiO_2/Si wafer for the growth of MoS_2, while mixed power of tungsten and tellurium is scattered on the wafer for the growth of WS_2. The addition of tellurium helps to accelerate the melting of tungsten powder during the growth (Fig. S4). Sulfur powder is put upstream within the low temperature zone. Argon is used to protect the system from oxygen and carry sulfur vapor from the upstream of the tube during the reaction. The difference in their nucleation and growth rate gives rise to sequential growth of MoS_2 and WS_2, instead of $Mo_xW_{1-x}S_2$ alloy, and the precise reaction temperature determines the structure of the final product: vertical stacked bilayers are preferred at ~850 ˚C, while in-plane lateral heterojunctions dominate when the synthesis was carried out at ~650˚C (see Methods for more details). A brief discussion of the possible mechanism of the temperature-selective growth is provided in the Supplementary Information. This simple, scalable growth process creates clean interfaces between the two monolayer components, which is advantageous over mechanical transfer of layers.

The morphology of the WS_2/MoS_2 vertical and in-plane heterostructures was examined by optical microscopy, scanning electron microscopy (SEM), and atomic force microscopy

(AFM). Figures 1A - 1D are the schematic and typical optical and SEM images of the vertical stacked heterostructures, showing individual WS_2/MoS_2 bilayer triangles and high yield of heterostructures. The bilayers can be easily distinguished from monolayers via optical contrast (Fig. 1B), with MoS_2 monolayers showing light purple color and the bilayer regions in much darker purple. The domain size of the bottom MoS_2 layer is typically larger than 10 μm. Both totally covered and partially covered WS_2/MoS_2 bilayer (Fig. S5) can be found, providing different geometries for device fabrication. The schematic and morphology of WS_2/MoS_2 in-plane heterostructures is shown in Figs. 1E - 1H, where the lateral interface between monolayer MoS_2 and WS_2 can be easily distinguished by the contrast difference. SEM and optical images shown in Fig. S6 demonstrate the high-yield of such in-plane heterostructure obtained from this growth method. The difference in bilayer or monolayer morphology of these two types of heterostructures is further verified by AFM images presented in Fig. S7.

Vertically stacked heterostructure - bilayer

The atomic structure of the vertical stacked WS_2/MoS_2 bilayers was studied by Z-contrast imaging and elemental mapping on an aberration-corrected STEM (see Methods). Figure 2A shows the morphology of the as-transferred stacked WS_2/MoS_2 heterostructure in a low-magnified Z-contrast image, where the image intensity is directly related to the averaged atomic number and the thickness of the sample[28-30]. A WS_2 monolayer would, therefore, display higher image contrast than a MoS_2 monolayer, while the image intensity from the bilayer heterostructure is roughly the sum of that from its two monolayer components. In order to highlight the different regions in the sample, the image in Fig. 2A is shown in a false color scale. Most of the sample is covered by continuous bilayer heterostructure (orange region), while at some intentionally induced broken edges (see Methods) both of the individual monolayers can be identified (with MoS_2 shown in blue and WS_2 shown in green). Figure 2B shows a magnified image of the region highlighted in Fig. 2A. The obvious contrast step across the two individual layers, as shown by the image intensity line profile in Fig. 2C, demonstrates the presence of separated MoS_2 and WS_2 monolayers instead of a homogenous $Mo_xW_{1-x}S_2$ alloy. Elemental mapping of Mo, W and S (Figs. 2D and S8) from

the same region unambiguously confirms that MoS_2 and WS_2 are well separated into two atomic layers, forming vertical bilayer heterostructures.

Figures 2E and 2F show atomic resolution Z-contrast images from the bilayer region and a step edge of the WS_2/MoS_2 heterostructure, respectively. The alternative bright and dark atomic column arranging in the hexagonal lattice suggests the as-grown stacked WS_2/MoS_2 heterostructure preserves the 2H stacking, where the bright and dark columns are W and Mo atom aligned with a S_2 column, respectively, as illustrated in Fig. 2G. The WS_2/MoS_2 heterostructure grown by our one-step growth method is found to have predominantly the 2H stacking, which exemplifies the advantage of this direct growth method over mechanical transfer method where the stacking orientation of the heterostructure cannot be well controlled. As a side note, Mo substitution in the WS_2 layer can be occasionally observed, as indicated by the reduced contrast at the W atomic sites (green arrows in Fig. 2E and the associated intensity line profile). Similarly, some trace amount of W atoms is also found to substitute into the MoS_2 layer (Fig. 2F). However, the substitution is at a fairly low concentration (~ 3%, see Fig. S9 for details), which would only have minimum effect on the properties of the MoS_2 and WS_2 monolayers.

Raman and PL spectroscopy were used to further characterize the vertical bilayer heterostructure. As shown in Figs. 3A and 3B, Raman spectra collected from the light purple area (points 1 and 2) show only the E' (at 383.9 cm^{-1}) and A_1' (at 405.3 cm^{-1}) peaks of MoS_2 monolayer[8,9], confirming the bottom layer is MoS_2[31]. In the bilayer region (point 3 and 4 in the dark purple area), however, two additional peaks located at 356.8 cm^{-1} and 418.5 cm^{-1} are observed, which can be assigned to the overlapping 2LA(M) & E' and A_1' modes, respectively, of the top WS_2 monolayer[6,32] (details in Fig. S10). Raman intensity mapping using the MoS_2 E' mode at 384cm^{-1} and the WS_2 E' mode at 357cm^{-1} further demonstrate the formation of WS_2/MoS_2 bilayer stacks, as shown in Figs. 3C and 3D.

The PL spectra (Fig. 3F) acquired from the monolayer region (points 1 and 2 in Fig. 3E) show only a strong peak at the wavelength of 680 nm, corresponding to the 1.82 eV direct excitonic

transition energy in monolayer MoS_2. However, on the bilayer region (points 3 and 4), three prominent peaks are observed at the wavelength of 630 nm, 680 nm, and 875 nm, corresponding to the excitonic transition energy of 1.97 eV, 1.82 eV, and 1.42 eV, respectively. The peaks at 630 nm (1.97 eV) and 680 nm (1.82 eV) can be attributed to the direct excitonic transition energy in the top WS_2 and bottom MoS_2 monolayer, respectively. It has been reported that the increased indirect excitonic transition in multilayer WS_2 and MoS_2[7,33] can generate small peaks at similar lower transition energy range. The intensity of such indirect excitonic peaks, however, is more than three orders of magnitude lower than the direct excitonic peak from monolayers. The comparable intensity of the peak at 875 nm to that of its individual monolayer components observed in our bilayer sample, as shown in Fig. 3F, indicates a possible direct excitonic transition at this energy range. Such strong direct excitonic peak at 875 nm (1.42 eV) is indeed observed for the first time in this bilayer heterostructure. This experimental observation is consistent with previous theoretical calculations, which suggest the coupling between the WS_2 and MoS_2 layers leads to a new direct bandgap with reduced energy.[25,26] Figure S11 shows the PL intensity mapping at 875 nm, confirming the intensity are localized at the bilayer region. Notably, the PL signal from MoS_2 at 680 nm shows a localized enhancement near the step edges between the monolayer and bilayer region, as shown in Fig. 3G and further illustrated by the PL intensity line profile shown in Fig. S12. The PL enhancement is also demonstrated by analyzing the PL spectra extracted from the step edge region (point 1) and the edge of the MoS_2 monolayer (point 2 in Fig. 3E), showing almost twice difference in intensity. This step-edge enhancement is distinctly different from the previous reported edge-enhanced[6] or homogeneous[34] PL response in monolayer TMDs, and may be caused by the interaction between the MoS_2 and WS_2 layers.

As a comparison, Raman and PL measurements were also performed on stacked WS_2/MoS_2 heterostructure, made by the commonly-used mechanical transfer method, and on CVD grown MoS_2 and WS_2 bilayer (Fig. 3H and S13). Although the Raman spectra are similar to the WS_2/MoS_2 bilayer from direct growth (Fig. S13), the additional PL peak at 875 nm, originated from interlayer excitonic transition[25,26], is absent in the PL spectra from the mechanically transfer stacked bilayer sample, presumably due to contaminations at the

interface during the mechanical transfer of the two layers. This new 875 nm peak should also be observable in transferred layers if a contamination-free interface could be achieved. These results highlight the advantage of using our CVD method for the direct growth of crystalline heterostructures, in which layer transfers are not needed and clean interface could be readily obtained. In addition, the 1.82 eV (680 nm) and 1.97 eV (630 nm) PL peaks observed in the stacked WS_2/MoS_2 bilayer are almost vanished in CVD-grown MoS_2 bilayer and WS_2 bilayer.[7] This observation suggests that the MoS_2 and WS_2 layers in the bilayer heterostructure, on one hand, behave as individual monolayers, and, on the other hand, generate new functionalities (a new direct band gap) of WS_2/MoS_2 heterostructure via interlayer coupling owing to the clean interface.

In order to illustrate the high quality of the CVD-grown heterostructures, we demonstrate high-mobility back-gating vertically stacked WS_2/MoS_2 field-effect transistors (FETs) (Fig. 3I, Fig. S14). As FETs, the ON/OFF ratio is larger than 10^6, and the estimated mobility (See supporting information) ranges from 15 to 34 $cm^2V^{-1}s^{-1}$, which is much higher than the average mobility of the monolayer MoS_2 (4.5 $cm^2V^{-1}s^{-1}$)[8,9], MoS_2 bilayer (5.7 $cm^2V^{-1}s^{-1}$) and WS_2/MoS_2 bilayer made by transfer method (0.51 $cm^2V^{-1}s^{-1}$), thus suggesting that the clean interface between WS_2 and MoS_2 is important for achieving a high device performance. The poor FET performance WS_2/MoS_2 bilayer made by transfer method is possibly due to the presence of unwanted species trapped between layers.

In-plane heterostructure

The lateral interface between WS_2 and MoS_2 within the in-plane connected heterostructure appears as straight lines in triangular shape in the optical images (Figs. 1E-1H), thus suggesting that the lateral epitaxy of WS_2 on MoS_2 edge occurs preferentially along the zigzag direction. Such assessment provides a macroscopic view of the WS_2/MoS_2 planar heterojunctions; however, the detailed atomic structure can only be revealed by high resolution STEM Z-contrast imaging. Figure 4A shows a Z-contrast image of the lateral interface, where W atoms display much higher image intensity than the Mo atoms. A series of sharp zigzag step interfaces can be easily identified along the overall-straight WS_2/MoS_2

lateral junction. An atomically sharp interface is consistently observed. Figure 4B shows another atomically sharp interface along the zigzag direction, where all atomic columns are directly visible. Careful examination of this STEM image reveals that the WS_2 and MoS_2 domains connect seamlessly at the interface into a single hexagonal monolayer lattice and share the same crystal orientation, as demonstrated in Fig. 4B (atomic model provided in Fig. S15). The formation of such atomically coherent interface is a strong indication of lateral expitaxy growth in which the WS_2 monolayer grows directly from the fresh MoS_2 edges with atomic lattice coherence. Lateral expitaxy is also supported by the electron diffraction pattern (Fig. S16). The interfacial steps most likely originate from small fluctuations of the MoS_2 growth rate at the nm-scale, and their presence contributes to the overall roughness of the lateral WS_2/MoS_2 interface. We estimate the overall roughness of the WS_2/MoS_2 interface by the evolution of the local W concentration, integrated along individual atomic planes parallel to the overall interface, as presented in Fig. S17. The overall roughness of the lateral interface is estimated to be ~4 unit cells over a width of 15 nm (Figs. S17 and S18), and we expect that this could be further reduced by optimizing the CVD growth conditions.

Despite the small overall roughness due to interfacial steps, each individual WS_2/MoS_2 heterojunction along the zigzag direction is found to be atomically abrupt, as shown by the high magnification STEM Z-contrast images in Figs. 4B and 4C. The corresponding atomic model, obtained via atom-by-atom image quantification, clearly indicates the seamless connection and abrupt transition between the MoS_2 and WS_2 lattice within a single atomic row (Figs. S15 and S19). To the best of our knowledge, this is the first demonstration and direct visualization of an atomically abrupt lateral interface between two different 2D materials with atomic resolution. Besides the preferred zigzag interface, lateral junctions along the armchair direction are also occasionally observed in our sample, as shown in Fig. 4D and Fig. S20. Slight inter-diffusion of transition metal elements is often observed along such armchair interfaces, typically over a width of 1-3 unit cells (Figs. S19 and S20), presumably due to the relative low stability of the fresh armchair MoS_2 edges during the epitaxial growth of the WS_2 layer[35]. Nevertheless, our growth produces the highest quality 2D

in-plane heterostructures reported so far, with atomically coherent sharp interfaces, providing an excellent platform for studying intralayer coupling effect.

The lateral WS_2/MoS_2 interface was further studied by Raman and PL spectroscopy. Figure 5A shows an optical image of the WS_2/MoS_2 in-plane heterojunction used for Raman and PL characterization. Raman spectra (Fig. 5B) and mapping (Fig. 5C) at 351 cm^{-1} (yellow) and 381 cm^{-1} (purple) both confirm the formation of in-plane WS_2/MoS_2 heterostructure, with triangular monolayer MoS_2 domain as the core and WS_2 being the shell layer (individual mapping is shown in Fig. S21). Similarly, PL spectra acquired from the outer layer (point 1 in Fig. 5D) and inner layer (point 5 in Fig. 5D) show characteristic PL peaks of pristine monolayer WS_2 and MoS_2, respectively, and the PL intensity mapping using these two peaks also reveals the core-shell structure of this unique lateral heterostructure (Figs. 5F and S22). Note that due to the large laser spot size (~1 μm) used in our experiment, the lateral interface in the Raman and PL mappings appears a bit diffuse, and the Raman spectrum from the interface area correspond to signals from both sides of the atomically abrupt heterojunction.

Even though the lateral heterostructure has been revealed by STEM imaging to have sharp interfaces with very limited inter-diffusion, the PL peak position shifts continuously across the interface from 630 nm (for WS_2) to 680 nm (for MoS_2), as shown by the spectra presented in Fig. 5D. Noticeably, the PL spectrum acquired at the interface (point 3) shows a broad and strong peak at 650 nm (1.91 eV). The observed shift in peak position and changes in peak shape cannot be simply due to the large laser spot size that picks up averaged information from an ~1 μm^2 area, as illustrated by the distinct difference between the PL spectrum acquired at the interface (point 3) and the superposition of spectra from pure MoS_2 and pure WS_2 (Fig. 5E). Furthermore, PL intensity mapping at 650 nm (Fig. 5G) reveals that this strong PL response is localized at the lateral interface, and the intensity drops significantly at the intersections of these interfaces, which is consistent with the PL spectra presented in Fig. 5E. The shift of the PL peak to intermediate energies near the interface can be explained as follows. Excitons near the interface have wavefunctions that overlap the other side, which causes a shift that gradually evolves to the excitonic peak on the other side. When the laser

spot is focused on the interface, it generates excitons in the intermediate energies, resulting in the observed broad peak between the two pristine excitonic peaks. This observed peak contains contributions from excitons that have an electron predominantly on one side and the hole predominantly on the other side (such excitons also have an intermediate energy as discussed in Fig. S23 and S24).

To further assess the localized interfacial effect, we acquired high-resolution PL microscope image from the heterostructure as shown in Fig. 5H. Strong (around 40 times enhancement comparing to the pristine MoS_2 or WS_2) and highly localized (within 250 nm of FWHM) PL enhancement is clearly shown along the lateral interfaces. In comparison, the PL signals from pristine MoS_2 or WS_2 area are close to the background level from the SiO_2/Si substrate. Such localized interfacial excitonic enhancement may due to the strong built-in electric field at the atomically sharp interface originated from the type II band alignment, as confirmed by DFT calculations (Fig. S25). The interface serves as an enhanced excitonic recombination center, where the strong built-in electric field breaks the coherence of the electron-hole pairs generated in the vicinity of the interface, leading to their preferential recombination at the interface. In contrast, in the areas of "bulk" monolayer MoS_2 or WS_2, radiative recombination of excitons may be suppressed by non-radiative channels.

The lateral WS_2/MoS_2 heterostructures is further demonstrated to serve as intrinsic monolayer p-n junctions (Figs. 5I and S26) without external electrical tuning. The forward biased current is two orders of magnitude higher than the reversed one, implying a good rectification character unique in 2D electronics. Furthermore, under illumination, the lateral heterostructure shows clear photo-voltaic effect, which is also a solid evidence for the existence of a *p-n* junction (Fig. 5I). Such photo-voltaic effect is consistent with the band alignment calculations presented in Fig. S25. An open loop voltage of 0.12 V and close loop current of 5.7 pA is obtained. This is the first time that the *p-n* junction and photo-voltaic effect are achieved in monolayer materials without external gating[15-17].

In summary, we have demonstrated the growth of high-quality vertical and lateral WS_2/MoS_2 heterostructures with clean and atomically sharp interfaces. The well-defined, sharp and clean interfaces in these heterostructure allow us to explore new and controlled designs for 2D materials. The specific orientation relationships and ordering between the individual monolayer domains can lead to specific interface electronic properties which cannot be obtained in randomly assembled van der Waals hetero-materials. Such scalable methods to grow engineered 2D heterostructures could lead to interesting applications such as vertically stacked FET devices and planar monolayer devices. Combining both vertical and lateral 2D heterostructures opens up new possibilities to create novel architectures using 2D atomic layer building blocks.

References:

1 Kroemer, H. Heterostructure bipolar-transistors and integrated-circuits. *Proceedings of the Ieee* **70**, 13-25 (1982).

2 Ohno, Y. *et al.* Electrical spin injection in a ferromagnetic semiconductor heterostructure. *Nature* **402**, 790-792 (1999).

3 Novoselov, K. S. *et al.* Two-dimensional gas of massless Dirac fermions in graphene. *Nature* **438**, 197-200 (2005).

4 Dean, C. R. *et al.* Boron nitride substrates for high-quality graphene electronics. *Nature Nanotech.* **5**, 722-726 (2010).

5 Song, L. *et al.* Large scale growth and characterization of atomic hexagonal boron nitride layers. *Nano Lett.* **10**, 3209-3215 (2010).

6 Gutierrez, H. R. *et al.* Extraordinary room-temperature photoluminescence in triangular WS_2 monolayers. *Nano Lett.* **13**, 3447-3454 (2013).

7 Mak, K. F., Lee, C., Hone, J., Shan, J. & Heinz, T. F. Atomically thin MoS_2: a new direct-gap semiconductor. *Phys. Rev. Lett.* **105**, 136805 (2010).

8 Najmaei, S. *et al.* Vapour phase growth and grain boundary structure of molybdenum disulphide atomic layers. *Nature Mater.* **12,** 754-759 (2013).

9 van der Zande, A. M. *et al.* Grains and grain boundaries in highly crystalline monolayer molybdenum disulphide. *Nature Mater.* **12**, 554-561 (2013).

10 Britnell, L. *et al.* Field-effect tunneling transistor based on vertical graphene heterostructures. *Science* **335**, 947-950 (2012).

11 Gannett, W. *et al.* Boron nitride substrates for high mobility chemical vapor deposited graphene. *Appl. Phys. Lett.* **98**, 242105 (2011).

12 Geim, A. K. & Grigorieva, I. V. Van der Waals heterostructures. *Nature* **499**, 419-425 (2013).

13 Georgiou, T. *et al.* Vertical field-effect transistor based on graphene-WS_2 heterostructures for flexible and transparent electronics. *Nature Nanotech.* **8**, 100-103 (2013).

14 Yu, W. J. *et al.* Highly efficient gate-tunable photocurrent generation in vertical heterostructures of layered materials. *Nature Nanotech.* **8**, 952-958 (2013).

15 Pospischil, A., Furchi, M. M. & Mueller, T. Solar-energy conversion and light emission in an atomic monolayer p-n diode. *Nature Nanotech.* **9**, 257-261 (2014).

16 Baugher, B. W., Churchill, H. O., Yang, Y. & Jarillo-Herrero, P. Optoelectronic devices based on electrically tunable p-n diodes in a monolayer dichalcogenide. *Nature Nanotech.* **9**, 262-267 (2014).

17 Ross, J. S. *et al.* Electrically tunable excitonic light-emitting diodes based on monolayer WSe_2 p-n junctions. *Nature Nanotech.* **9**, 268-272 (2014).

18 Haigh, S. J. *et al.* Cross-sectional imaging of individual layers and buried interfaces of graphene-based heterostructures and superlattices. *Nature Mater.* **11**, 764-767 (2012).

19 Yang, W. *et al.* Epitaxial growth of single-domain graphene on hexagonal boron nitride. *Nature Mater.* **12**, 792-797 (2013).

20 Levendorf, M. P. *et al.* Graphene and boron nitride lateral heterostructures for atomically thin circuitry. *Nature* **488**, 627-632 (2012).

21 Liu, Z. *et al.* In-plane heterostructures of graphene and hexagonal boron nitride with controlled domain sizes. *Nature Nanotech.* **8**, 119-124 (2013).

22 Liu, L. *et al.* Heteroepitaxial growth of two-dimensional hexagonal boron nitride templated by

graphene edges. *Science* **343**, 163-167 (2014).

23 Han, G. H. *et al.* Continuous growth of hexagonal graphene and boron nitride in-plane heterostructures by atmospheric pressure chemical vapor deposition. *Acs Nano* **7**, 10129-10138 (2013).

24 Miyata, Y. *et al.* Fabrication and characterization of graphene/hexagonal boron nitride hybrid sheets. *Appl. Phys. Express* **5**, 085102 (2012).

25 Kosmider, K. & Fernandez-Rossier, J. Electronic properties of the MoS_2-WS_2 heterojunction. *Phys. Rev. B* **87**, 075451 (2013).

26 Terrones, H., Lopez-Urias, F. & Terrones, M. Novel hetero-layered materials with tunable direct band gaps by sandwiching different metal disulfides and diselenides. *Sci. Rep.* **3**, 1549 (2013).

27 Kang, J., Tongay, S., Zhou, J., Li, J. B. & Wu, J. Q. Band offsets and heterostructures of two-dimensional semiconductors. *Appl. Phys. Lett.* **102**, 012111 (2013).

28 Krivanek, O. L. *et al.* Atom-by-atom structural and chemical analysis by annular dark-field electron microscopy. *Nature* **464**, 571-574 (2010).

29 Zhou, W. *et al.* Intrinsic structural defects in monolayer molybdenum disulfide. *Nano Lett* **13**, 2615-2622 (2013).

30 Gong, Y. J. *et al.* Band gap engineering and layer-by-layer mapping of selenium-doped molybdenum disulfide. *Nano Lett.* **14**, 442-449 (2014).

31 Terrones, H. *et al.* New first order Raman-active modes in few layered transition metal dichalcogenides. *Sci. Rep.* **4**, 4215 (2014).

32 Berkdemir, A. *et al.* Identification of individual and few layers of WS_2 using Raman spectroscopy. *Sci Rep* **3**, 1755 (2013).

33 Zhao, W. J. *et al.* Evolution of electronic structure in atomically thin sheets of WS_2 and WSe_2. *Acs Nano* **7**, 791-797 (2013).

34 Peimyoo, N. *et al.* Nonblinking, Intense two-dimensional light emitter: monolayer WS_2 triangles. *Acs Nano* **7**, 10985-10994 (2013).

35 Wang, Z. *et al.* Mixed low-dimensional nanomaterial: 2D ultranarrow MoS_2 inorganic nanoribbons encapsulated in quasi-1D carbon nanotubes. *J. Am. Chem. Soc.* **132**, 13840-13847 (2010).

Acknowledgments

This work was supported by the Army Research Office MURI grant W911NF-11-1-0362, U.S. DOE grant DE-FG02-09ER46554 (JL, STP), a Wigner Fellowship through the Laboratory Directed Research and Development Program of Oak Ridge National Laboratory (ORNL), managed by UT-Battelle, LLC, for the U. S. DOE (WZ), the FAME Center, one of six centers of STARnet, a Semiconductor Research Corporation program sponsored by MARCO and DARPA, the U.S. Office of Naval Research MURI grant N000014-09-1-1066, NSF grant ECCS-1327093 and MOE Academic Research Fund (AcRF) Tier 1 RG81/12 project Singapore and Si-COE project, Singapore. This research was also supported through a user project supported by ORNL's Center for Nanophase Materials Sciences (CNMS), which is

sponsored by the Scientific User Facilities Division, Office of Basic Energy Sciences, U.S. DOE. This research used resources of the National Energy Research Scientific Computing Center, which is supported by the Office of Science of the US Department of Energy under Contract No.DE-AC02-05CH11231. This work was also supported by the Singapore National Research Foundation under NRF RF Award No. NRF-RF2013-08, the start-up funding from Nanyang Technological University (M4081137.070).

Author Contributions

Y.G. J.L. and X.W. contributed equally to this work. Y.G. designed the growth and carried out part of the characterizations. Y.G., X.W. and G.Y. worked on the growth. W.Z. and J.L. carried out STEM experiments. G.S. and S.L. made FET devices and carried out the electrical measurement. Z.L. performed part of the Raman and PL characterization. H.T., X.Z. and J.L carried out DFT calculations. Y.G., J.L., X.W., W.Z., Z.L., G.S., S.L. M.T., H.T. and P.M.A. analyzed the results and co-wrote the paper. All authors participated in discussions.

Additional information

Supplementary information is available in the online version of the paper. Reprints and permissions information is available online atwww.nature.com/reprints.

Correspondence and requests for materials should be addressed to W.Z. or P.M.A.

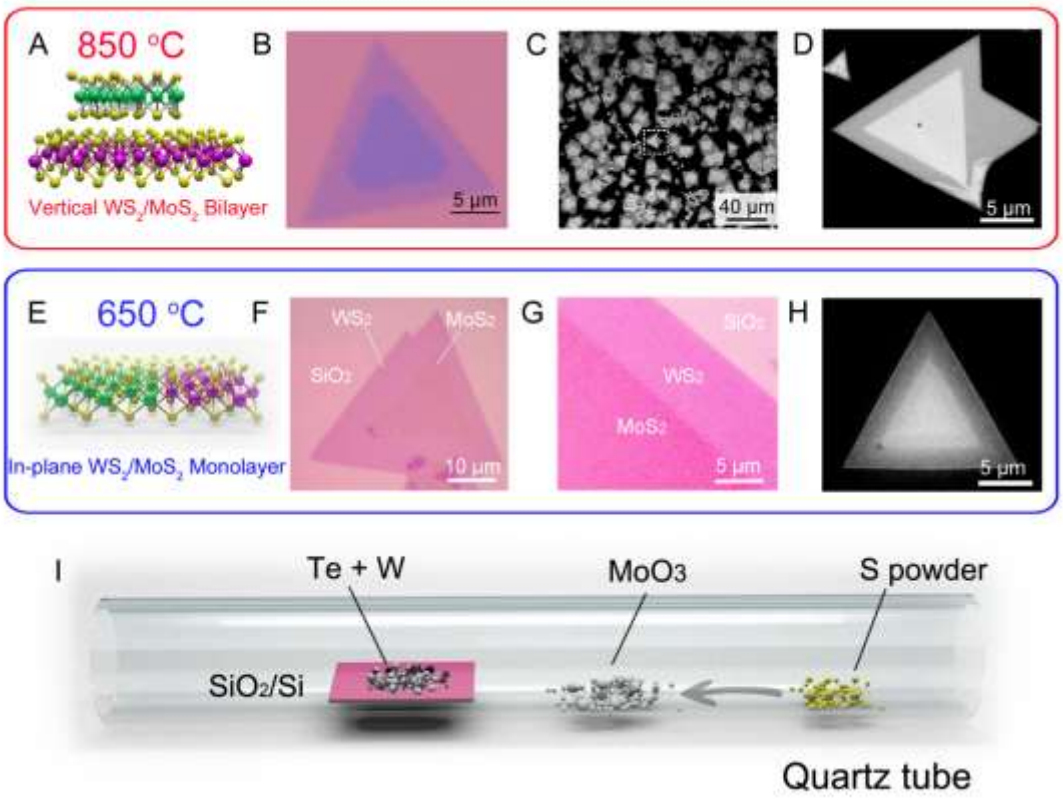

Figure 1. Schematic of the synthesis and the overall morphologies of the vertical stacked and in-plane WS_2/MoS_2 heterostructures. (A-D) Schematic, optical and SEM images of the vertical stacked WS_2/MoS_2 heterostructures synthesized at 850 ˚C, showing the bilayer feature and the high yield of the triangular heterostructures. (E-H) Schematic, optical and SEM images of the WS_2/MoS_2 in-plane heterojunctions grown at 650 ˚C. (G) is an optical image of the interface between WS_2 and MoS_2 with enhanced color contrast, showing the abrupt change of contrast at the interface. SEM images are presented in reverse contrast. The green, purple and yellow spheres in (A) and (E) represent W, Mo and S atoms, respectively. (I) Schematic of the synthesis process for both heterostructures.

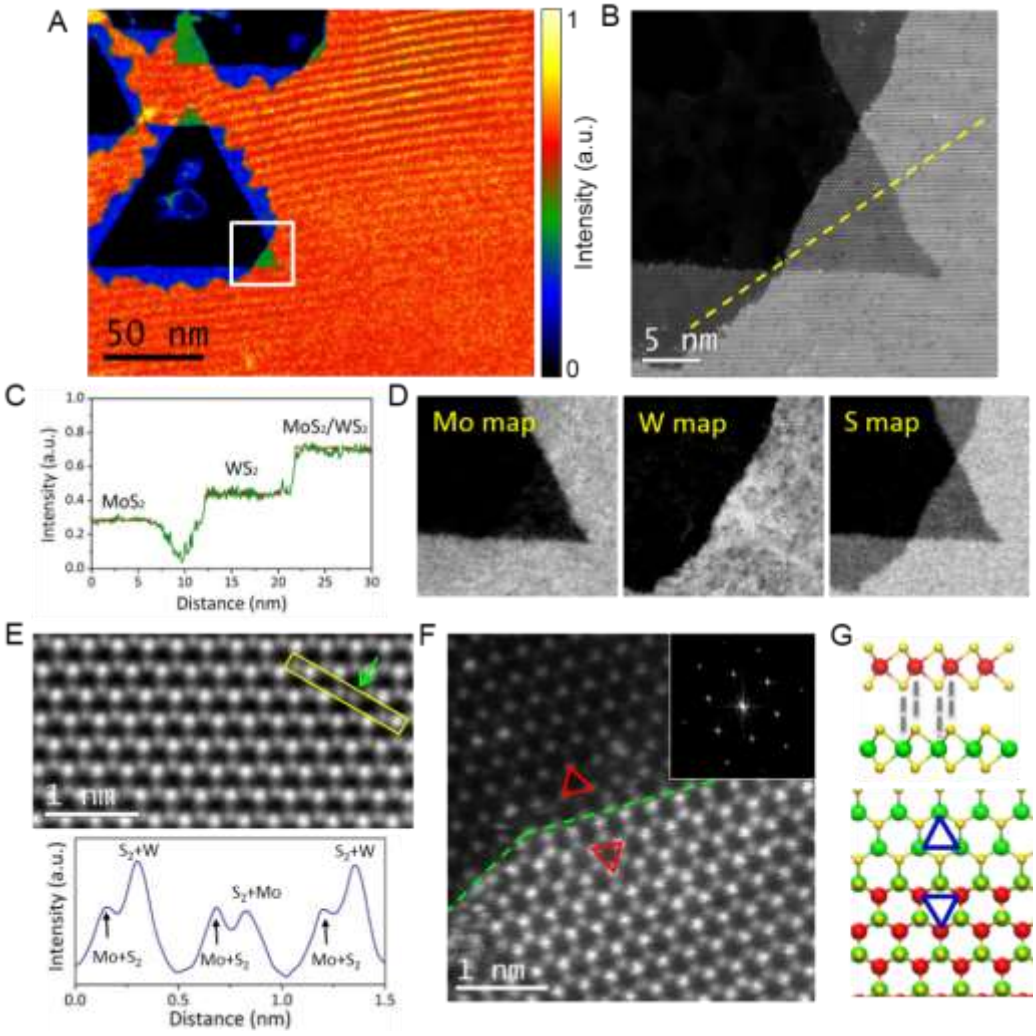

Figure 2. STEM-Z-contrast imaging and elemental mapping of the stacked WS_2/MoS_2 heterostructures. (A) Low-magnified false-colored Z-contrast image of the sample, where monolayer MoS_2 is shown in blue, monolayer WS_2 in green, and WS_2/MoS_2 bilayer in orange. (B) Zoom in view of the region highlighted in (A). (C) Z-contrast image intensity profile along the highlighted dashed line in (B), showing the distinct contrast variation among the different monolayers and bilayer region. (D) Elemental mapping of Mo, W, and S from the whole area shown in (B). (E) Z-contrast image of the bilayer region with 2H stacking orientation. The brighter columns are overlapping columns of W and S_2, while the less bright columns are overlapping of S_2 and Mo. The green arrow points to the atomic positions where W atom is replaced by Mo in the WS_2 layer, which has similar intensity to its neighboring site. Below: Image intensity profile acquired along the yellow rectangle in (E). (F) Z-contrast image of the step edge of the WS_2/MoS_2 bilayer. The green dash line highlights the step edge,

and the two triangles highlight the orientation of the MoS_2 and WS_2 layer, respectively. Inset: FFT of the Z-contrast image showing only one set of diffraction pattern. (G) Schematic of the 2H stacking in the stacked WS_2/MoS_2 heterostructure.

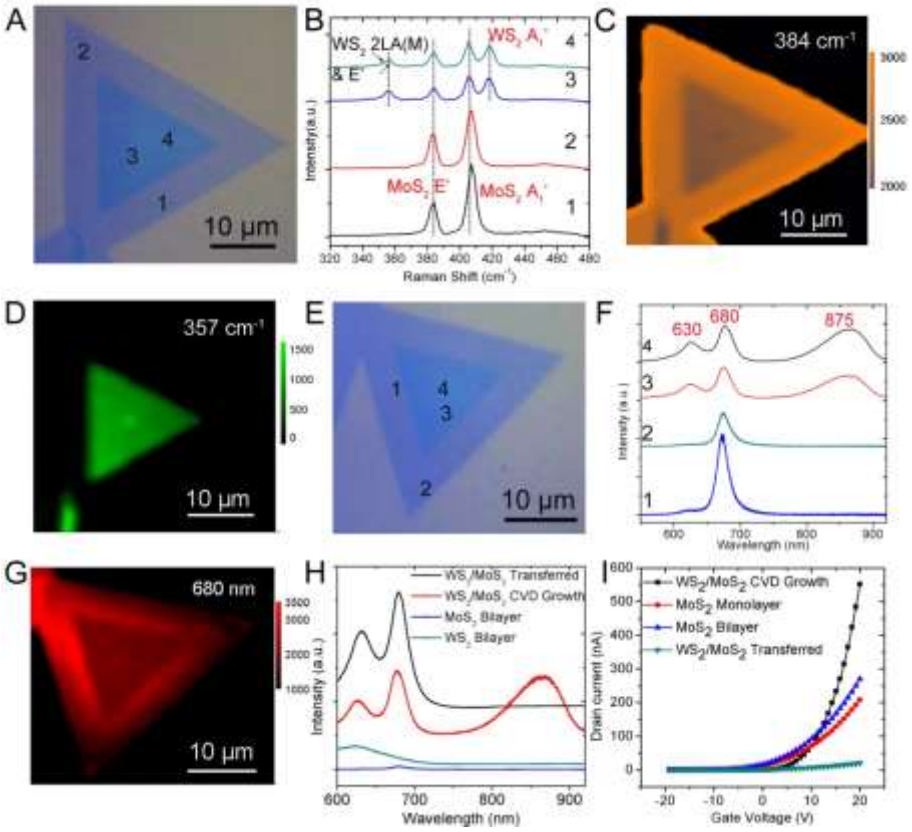

Figure 3. Raman and PL characterization of the WS_2/MoS_2 vertical heterostructure. (A) Optical image of a WS_2/MoS_2 heterostructure used for Raman characterization. (B) Raman spectra taken from the four points marked in (A), showing that the monolayer region is pure MoS_2, while the double layer area is the superposition of MoS_2 and WS_2 monolayers. (C, D) Raman intensity mapping at 384 cm^{-1} and 357 cm^{-1}, respectively. The lower Raman intensity at the center of the triangle in (C) is due to the coverage of WS_2. (E) Optical image of a WS_2/MoS_2 heterostructure used for PL characterization. (F) PL Spectra taken from the four points marked in (E), showing the characteristic MoS_2 PL peak at the monolayer region and three peaks at the bilayer region. (G) PL intensity mapping at 680 nm shows localized PL enhancement around the step edge of the bilayer region. (H) PL spectra of CVD-grown WS_2/MoS_2 bilayer, WS_2/MoS_2 bilayer made by mechanical transfer, and CVD-grown MoS_2 and WS_2 bilayers, respectively. All spectra were taken at the same laser intensity and plotted

to the same scale. The PL peak at 875 nm is absent at the mechanically transferred bilayer sample, and the bilayer MoS_2 and WS_2 have very weak PL response due to their indirect bandgap. (I) Typical plot of gating voltage versus source/drain current of CVD-grown WS_2/MoS_2 bilayer, mechanically transferred WS_2/MoS_2 bilayer, MoS_2 bilayer, and monolayer MoS_2, respectively, demonstrating that the CVD-grown WS_2/MoS_2 bilayer has the best performance.

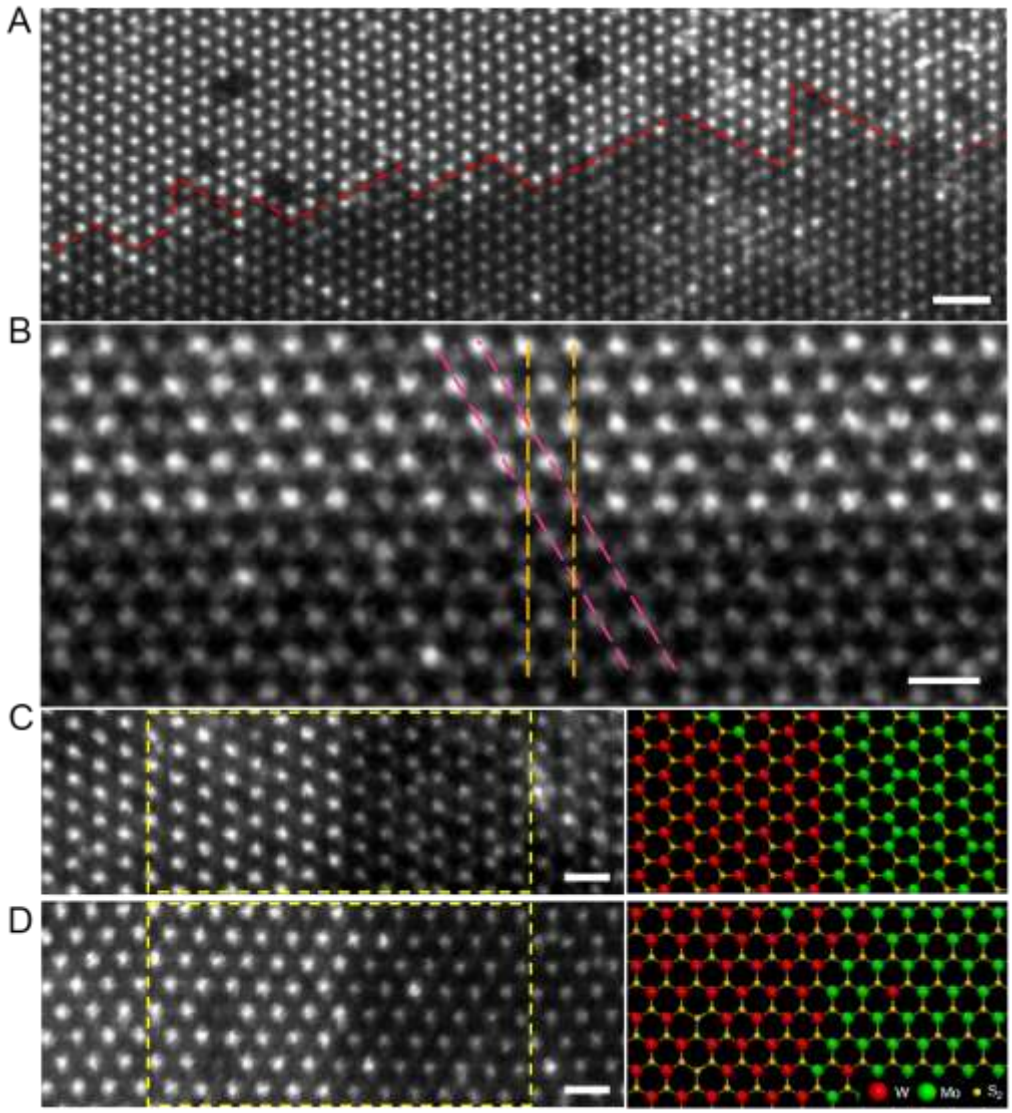

Figure 4. Atomic structure of the lateral heterojunctions between WS_2 and MoS_2 monolayers. (A, B) Atomic resolution Z-contrast STEM images of the in-plane interface between WS_2 and MoS_2 domains. Small roughness resulting from interfacial steps can be seen in A. The red dashed lines highlight the atomically sharp interface along the zigzag-edge direction. The orange and pink dashed lines depict the atomic planes along the arm-chair and zigzag directions, respectively, indicating the WS_2 and MoS_2 domains share the same crystal orientation. (C, D) Atomic resolution Z-contrast images of the atomically sharp lateral interfaces along the zigzag (C) and armchair (D) directions. The atomic models on the right correspond to the structure in the highlighted regions. Scale bars: (A) 1 nm; (B-D) 0.5 nm.

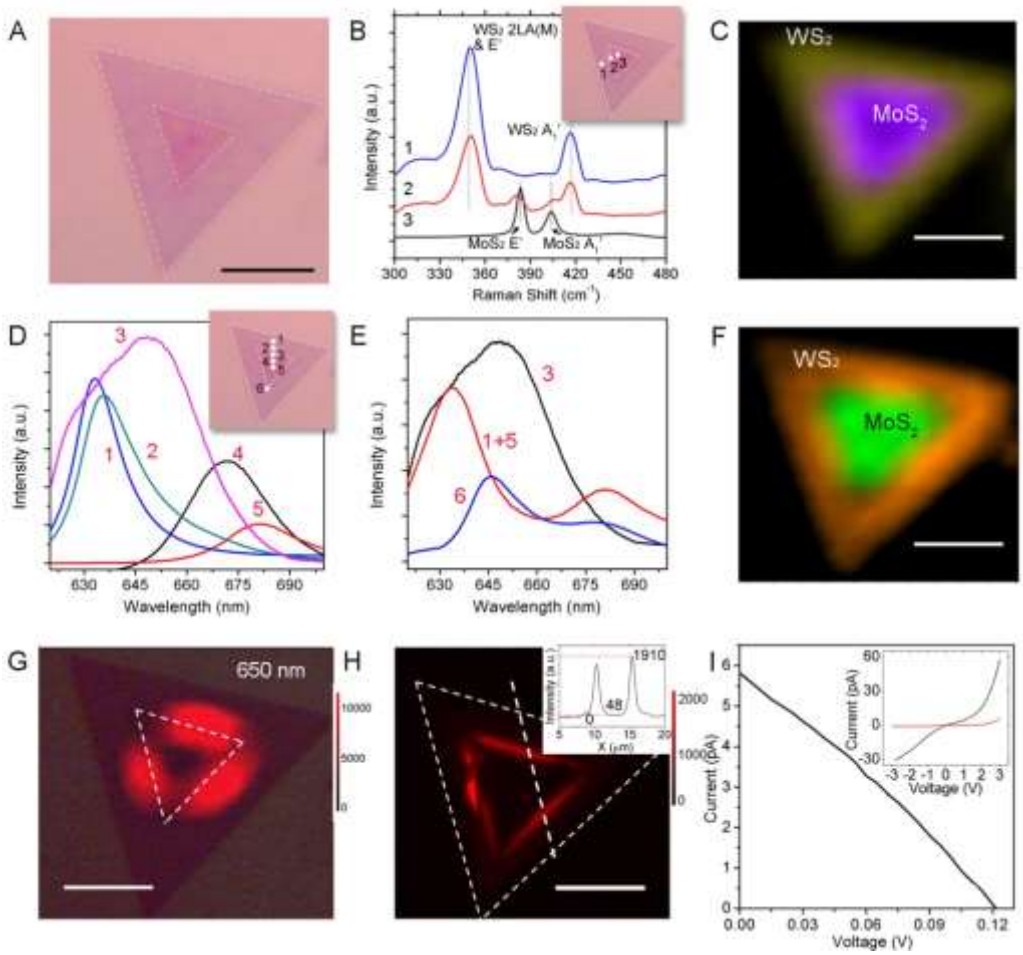

Figure 5. Raman and PL characterizations of in-plane WS_2/MoS_2 heterojunction. (A) Optical microscopy image of a triangular in-plane WS_2/MoS_2 heterojunction for Raman and PL characterization. (B) Raman spectra taken from the points marked by 1-3 in its inset, showing characteristic WS_2 (point 1) and MoS_2 (point 3) peaks in the outer and inner triangles, respectively, and their superposition at the interface region (point 2). (C) Combined Raman intensity mapping at 351 cm^{-1} (yellow) and 381 cm^{-1} (purple), showing the core-shell structure with WS_2 as the shell and MoS_2 as the core. (D) PL spectra of the points marked by 1-5 in its inset. The peak positions for spectra 1 and 5 are 630 nm and 680 nm, respectively, indicating pure WS_2 and pure MoS_2. The PL peak shifts as approaching the interface (points 2 and 4). At the interface (point 3), a stronger broad peak at 650 nm shows up. (E) PL spectra at the interface (point 3), at the intersection of interface (point 6) and the superposition of spectra from pure MoS_2 (point 5) and pure WS_2 (point 1). (F) Combined PL intensity mapping at 630 nm (orange) and 680 nm (green). (G) PL intensity mapping at 650 nm, showing localized response around the interface. The optical image with interface highlighted

is overlaid in (G). (H) PL microscope image of the same region in (G) in false color, showing strong localized PL enhancement at the interface. Inset is the corresponding intensity profile along the marked dash line, and the corresponding intensities of interface, pristine MoS_2 and back ground are marked. (I) Photo-voltaic effect of the in-plane heterojunction. Inset is the typical I-V curve of the junction with (black) and without (red) illumination, showing the p-n junction behavior. Scale bar: (A, C, F, G, H) 10 μm.